JOURNAL OF THE AMERICAN CHEMICAL SOCIETY

pubs.acs.org/JACS

Article

Amorphous Oxyhalide Matters for Achieving Lithium Superionic Conduction

Shumin Zhang,◆ Feipeng Zhao,◆ Lo-Yueh Chang, Yu-Chun Chuang, Zhen Zhang, Yuanmin Zhu, Xiaoge Hao, Jiamin Fu, Jiatang Chen, Jing Luo, Minsi Li, Yingjie Gao, Yining Huang, Tsun-Kong Sham, M. Danny Gu,* Yuanpeng Zhang,* Graham King,* and Xueliang Sun*

Cite This: J. Am. Chem. Soc. 2024, 146, 2977−2985

Read Online

ACCESS | Metrics & More | Article Recommendations | Supporting Information

ABSTRACT: The recently surged halide-based solid electrolytes (SEs) are great candidates for high-performance all-solid-state batteries (ASSBs), due to their decent ionic conductivity, wide electrochemical stability window, and good compatibility with high-voltage oxide cathodes. In contrast to the crystalline phases in halide SEs, amorphous components are rarely understood but play an important role in Li-ion conduction. Here, we reveal that the presence of amorphous component is common in halide-based SEs that are prepared via mechanochemical method. The fast Li-ion migration is found to be associated with the local chemistry of the amorphous proportion. Taking Zr-based halide SEs as an example, the amorphization process can be regulated by incorporating O, resulting in the formation of corner-sharing Zr−O/Cl polyhedrons. This structural configuration has been confirmed through X-ray absorption spectroscopy, pair distribution function analyses, and Reverse Monte Carlo modeling. The unique structure significantly reduces the energy barriers for Li-ion transport. As a result, an enhanced ionic conductivity of $(1.35 \pm 0.07) \times 10^{-3}$ S cm^{-1} at 25 °C can be achieved for amorphous $Li_3ZrCl_4O_{1.5}$. In addition to the improved ionic conductivity, amorphization of Zr-based halide SEs via incorporation of O leads to good mechanical deformability and promising electrochemical performance. These findings provide deep insights into the rational design of desirable halide SEs for high-performance ASSBs.

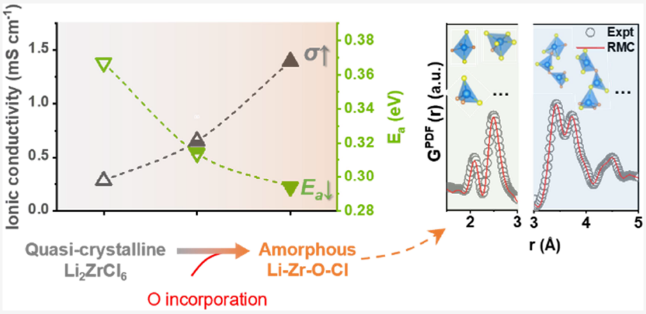

1. INTRODUCTION

Green mobility plays a crucial role in achieving the objectives of the clean energy revolution. The transition to electric vehicles heavily depends on the development of advanced battery technologies and efficient production capabilities.[1−3] All-solid-state batteries (ASSBs) with solid electrolytes (SEs) and potentially employing alkaline metal anodes and high-voltage cathodes are believed to provide an opportunity for achieving excellent safety and high-energy density.[4−6] In ASSBs, SEs are in direct contact with electrode materials, replacing the flammable organic liquid electrolytes and inert separators. The advancement of SEs governs the development of ASSBs.[7−10]

Among different categories of SEs (e.g., oxides, sulfides, hydrides, polymers, hybrids, etc.), halide-based SEs have drawn increasing attention due to their high ionic conductivities (up to 10^{-2} S cm^{-1}), good anti-oxidation stability (over 4 V vs Li^+/Li), and decent mechanical deformability.[11−14] Since Panasonic reported Li_3YCl_6 and Li_3YBr_6 in 2018,[15] the ternary halides (Li−M−X, M = metal cation, X = halogen anion) have been widely reported.[16−20] Most ternary halide-based SEs are in crystalline phases, which show either hexagonal-close-packed (*hcp*) or cubic-close-packed (*ccp*) anion sublattices.[10] High crystallinity is generally pursued to ensure good ionic conductivity of *ccp* structured SEs, such as representative Li_3YBr_6,[15] Li_3InCl_6,[16,21] Li−Sc−Cl,[17,22] etc. A ball milling (BM) plus post-annealing or co-melting process contributes to form high-crystalline (*hc*) phases with the optimized ionic conductivity. However, for some halides, such as Li_3YCl_6,[15] Li_3ErCl_6,[23] and Li_2ZrCl_6,[24,25] their low-crystalline (*lc*) phases from a mechanochemical (e.g., high-energy BM) process possess decent ionic conductivities in the order of 10^{-4} S cm^{-1}, while a post-annealing treatment reduces the ionic conductivity (under the circumstance of maintaining the same crystalline phase). Possible explanations, such as cation sites disorder[23,26] and stacking faults[27] have been proposed. Nevertheless, these understandings based on crystallography knowledge are inadequate to cover all the behaviors of halide SEs synthesized by the one-step mechanochemical method. Discussions about

Received: July 10, 2023
Revised: January 6, 2024
Accepted: January 9, 2024
Published: January 29, 2024

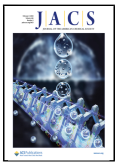

ACS Publications

https://doi.org/10.1021/jacs.3c07343

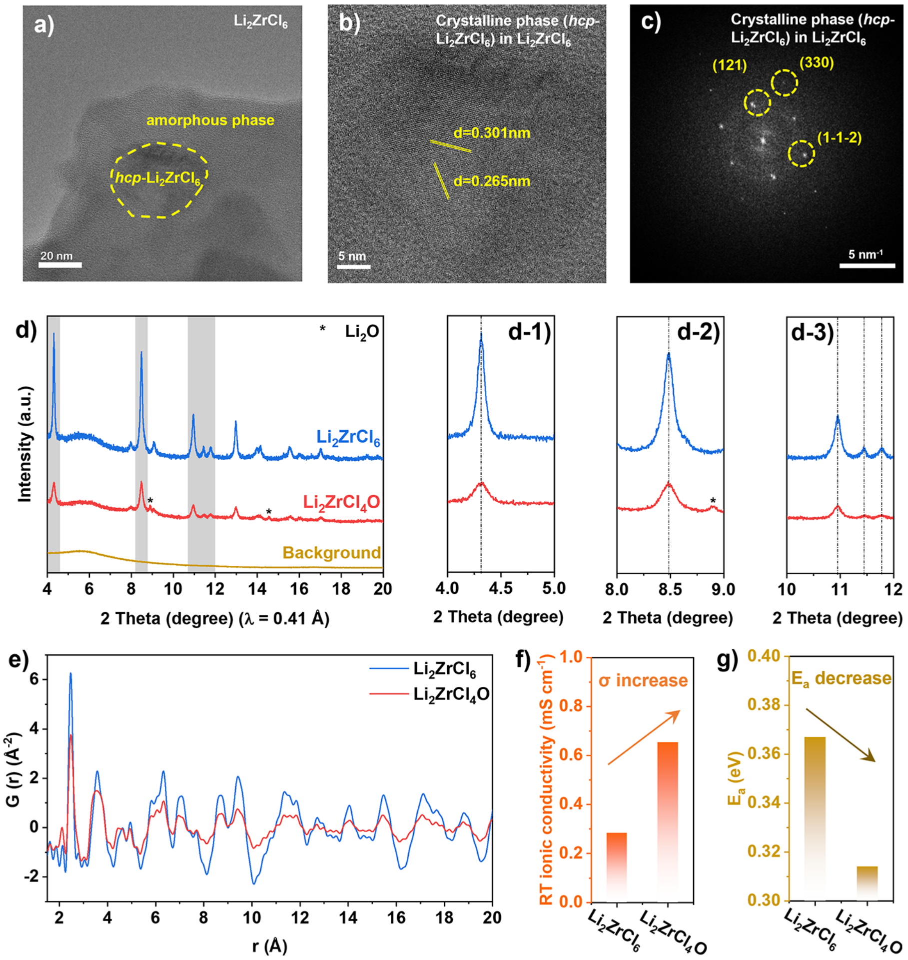

Figure 1. (a) Representative cryo-TEM image of Li_2ZrCl_6. (b) High-resolution TEM image of the crystalline component (*hcp*-Li_2ZrCl_6) in Li_2ZrCl_6 and (c) the corresponding Fast-Fourier-transform (FFT) pattern. (d) SXRD patterns of the Li_2ZrCl_6 and Li_2ZrCl_4O powders with magnified regions of (d-1) 4−5°, (d-2) 8−9°, and (d-3) 10−12°. Background signal comes from the quartz capillary that we used during the test. (e) Comparison of PDF ($\lambda \approx 0.23$ Å) patterns for Li_2ZrCl_6 and Li_2ZrCl_4O materials. Comparisons of (f) ionic conductivities (RT is 25 °C) and (g) activation energies for Li_2ZrCl_6 and Li_2ZrCl_4O SEs.

the non-negligible amorphous proportion in the obtained halide SEs[28] are usually omitted. Wang et al. found the existence of a significant amount of nonperiodic components in Li_2ZrCl_6 halide SEs and speculated that the decent ionic conductivity of Li_2ZrCl_6 was originated from this nonperiodic structure rather than the specific crystalline phase(s).[25]

Indeed, very recently, amorphous halide SEs have gradually attracted attention. Ishiguro et al. reported an amorphous $LiTaCl_6$ SE by using a long-duration (>120 h) BM process,[29] which shows excellent ionic conductivity of over 10^{-2} S cm^{-1}. Our group reported a series of amorphous Li−M−O−Cl (M = Ta, Hf) oxychloride SEs via constructing mixed-anion (Cl and O) frameworks.[30] The highly disordered M−O/Cl arrangements with corner-sharing of the O and rich terminal Cl are regarded as the main reasons for the fast Li-ion transport (up to 6.6×10^{-3} S cm^{-1} at 25 °C). Although these reported amorphous halide SEs appear promising, either careful regulation of crystalline-to-amorphous transition, or the relevance between the structure and ionic conduction was rarely established. Nevertheless, solving these issues is essential to realize controllable synthesis of desirable halide SEs.

In this work, taking the cost-effective Zr-based halide SEs as an example, we first reveal the quasi-amorphous nature of the Li_2ZrCl_6 synthesized from a typical BM method. Through O incorporation, we further manipulate the amorphization of the Zr-based halide SEs (amorphous content: 69.1−89.5%), and understand the correlation between the enhanced ionic conduction and amorphous component. As a result, an optimized $Li_3ZrCl_4O_{1.5}$ amorphous SE shows a high ionic conductivity of $(1.35 \pm 0.07) \times 10^{-3}$ S cm^{-1} at 25 °C, which is an order of magnitude increase compared to the quasi-crystalline Li_2ZrCl_6 (10^{-4} S cm^{-1} level). The structure of $Li_3ZrCl_4O_{1.5}$ amorphous SE is investigated in depth. Particularly, the combined synchrotron-based spectroscopy and Reverse Monte Carlo (RMC) modeling analyses contribute to disclose the amorphous local structure and its close correlation to the high ionic conductivity. Finally, the practicality of the regulated amorphous Zr-based halide SEs is demonstrated in high-performance ASSBs with conventional layered oxide cathode materials.

2. RESULTS AND DISCUSSION

The base material, Li_2ZrCl_6, was synthesized via a BM process (see experimental section for details). As shown in Figure S1, the synchrotron-based X-ray diffraction (SXRD) pattern of the as-prepared Li_2ZrCl_6 can be indexed to a trigonal phase with an *hcp* anionic sublattice. Broad diffraction peaks were observed. This phenomenon also occurs to some other halide

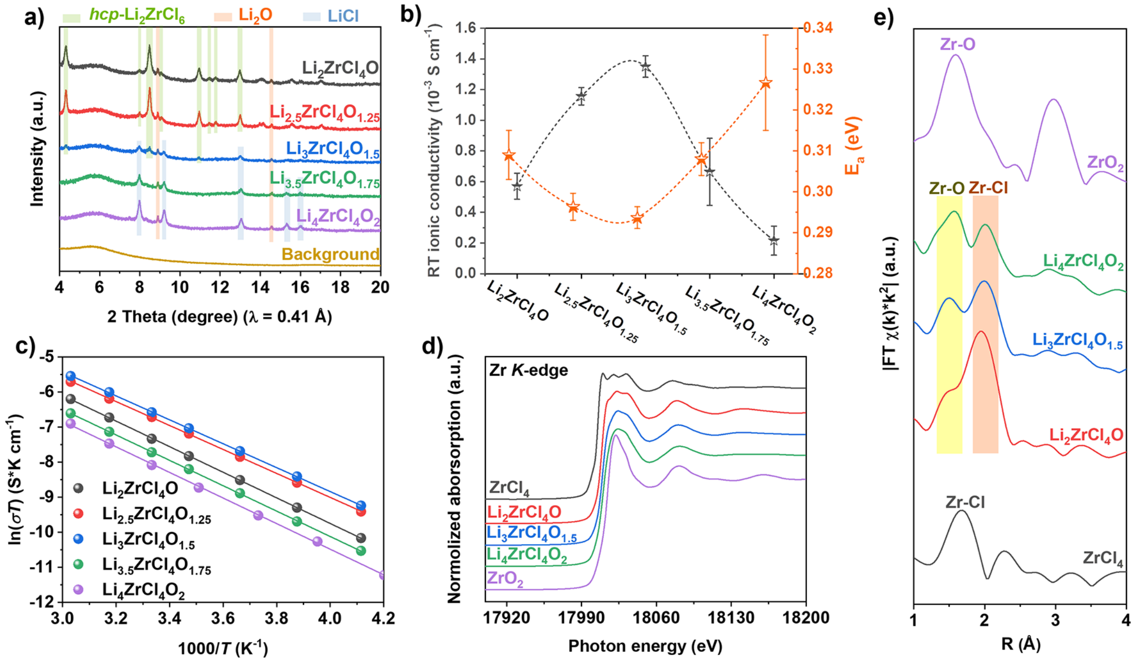

Figure 2. (a) SXRD patterns of the $Li_{2+2x}ZrCl_4O_{1+x}$ SEs (x = 0, 0.25, 0.5, 0.75, and 1). (b) Comparison of ionic conductivities and activation energies of the $Li_{2+2x}ZrCl_4O_{1+x}$ SEs. (c) Arrhenius plots of the $Li_{2+2x}ZrCl_4O_{1+x}$ SEs. (d) XANES and (e) FT-EXAFS spectra of the Li_2ZrCl_4O, $Li_3ZrCl_4O_{1.5}$, and $Li_4ZrCl_4O_2$ SEs at the Zr K-edge, respectively. $ZrCl_4$ and ZrO_2 are reference samples.

SEs prepared by the one-step BM method, such as Li_3YCl_6 and Li_3ErCl_6.[15,23] Figure 1a−c shows the cryogenic transition electron microscopy (cryo-TEM) characterizations of the Li_2ZrCl_6 powder. Crystalline *hcp*-Li_2ZrCl_6 grains were embedded in highly disordered regions. The amorphous proportion may be originated from the mechanochemical synthesis process, in which mechanical energy is transformed into pulverization chemical energy to "thermal quench" the powder samples locally and rapidly with the formation of amorphous regions.[31] In the present study, we used the internal standard method to figure out that the amorphous content in the Li_2ZrCl_6 SE was 46.0% (Figure S2), which was similar to the previous report (∼48%).[32] As we previously reported superionic amorphous Li−M−O−Cl (M = Ta, Hf) halide SEs,[30] here we further utilize the mixed-anion strategy with systematic O introduction to regulate the amorphization degree of the Zr-based halide SEs and to study the relationship with their ionic conduction. For a base formula of Li_2ZrCl_6, partial substitution of Cl by O was achieved by using Li_2O in place of the LiCl starting material while maintaining the Li/Zr molar ratio of 2:1. The resultant Li_2ZrCl_4O exhibited a similar diffraction pattern to that of Li_2ZrCl_6 except for a small amount of residual Li_2O (Figure 1d). Comparing Li_2ZrCl_4O to Li_2ZrCl_6, theoretically, a considerable amount of the Cl was replaced by O (33.3%), which showed a higher O substitution percentage compared to previous reports about doping O (8−21%) in the Li_2ZrCl_6 SEs.[32−34] Nevertheless, although there is a big difference in radius between Cl^- (181 pm) and O^{2-} (140 pm), a nonobservable peak shift appeared in the Li_2ZrCl_4O SE (see the magnified regions from Figure 1d-1−d-3). This indicated that O was not doped into the structure of crystalline *hcp*-Li_2ZrCl_6 but altered the properties of the amorphous phase that increased to 69.1% in Li_2ZrCl_4O SE. The incorporation of the O into the amorphous portion of the Li_2ZrCl_4O SE was further verified by conducting electron energy loss spectroscopy (EELS) element mapping as displayed in Figure S3.

Figure 1e shows the pair distribution function (PDF) profiles of Li_2ZrCl_6 and Li_2ZrCl_4O materials. Compared with Li_2ZrCl_6, the reduced peak intensity and widened peak width for Li_2ZrCl_4O suggested a higher amorphous content with disordered structures inside. Furthermore, combined with wavelet-transformed (WT) extended x-ray absorption fine structure (EXAFS) and Fourier-transformed (FT) EXAFS fitting results (Figure S4 and Table S1), an emerged peak at 2.09 Å in the Li_2ZrCl_4O PDF profile can be attributed by Zr−O bonding. An asymmetric peak between 3 and 4 Å corresponds to connection diversity between Zr-centered polyhedrons. More importantly, the dominance of the amorphous content in the Li_2ZrCl_4O sample can be verified by measuring the ionic conductivity and activation energy (Figure S5). As displayed in Figure 1f,g, after tuning and increasing the amorphous content via O participation with the formation of Li_2ZrCl_4O, there was a double increase in the ionic conductivity (at 25 °C), accompanied with a decreased activation energy.

We then tuned the composition of the Zr-base halide SEs to further elaborate the relation between amorphization and ionic conduction. A series of $Li_{2+2x}ZrCl_4O_{1+x}$ SEs (x = 0, 0.25, 0.5, 0.75, and 1) was synthesized from various stoichiometric ratios of $ZrCl_4$ and Li_2O. Figure 2a shows the SXRD patterns. The detailed quantification of the phase compositions for each $Li_{2+2x}ZrCl_4O_{1+x}$ SE was obtained by refinement (Figure S6), and the results are summarized in Figure S7. Increasing the ratio of Li_2O reduced the formation probability of crystalline *hcp*-Li_2ZrCl_6. Minimal impurities of *hcp*-Li_2ZrCl_6, Li_2O, and LiCl were achieved for $Li_{2+2x}ZrCl_4O_{1+x}$ when x = 0.5, showing the highest degree of amorphization (89.5%) with a further improved O substitution of 42.9% comparing to Li_2ZrCl_4O (33.3% of O substitution). EELS mapping for the highly amorphous $Li_3ZrCl_4O_{1.5}$ sample suggested that the homogeneous dispersion of Zr, Cl, O, and Li elements constitutes the amorphous component (Figure S8). It is noted that such weak

https://doi.org/10.1021/jacs.3c07343
J. Am. Chem. Soc. 2024, 146, 2977−2985

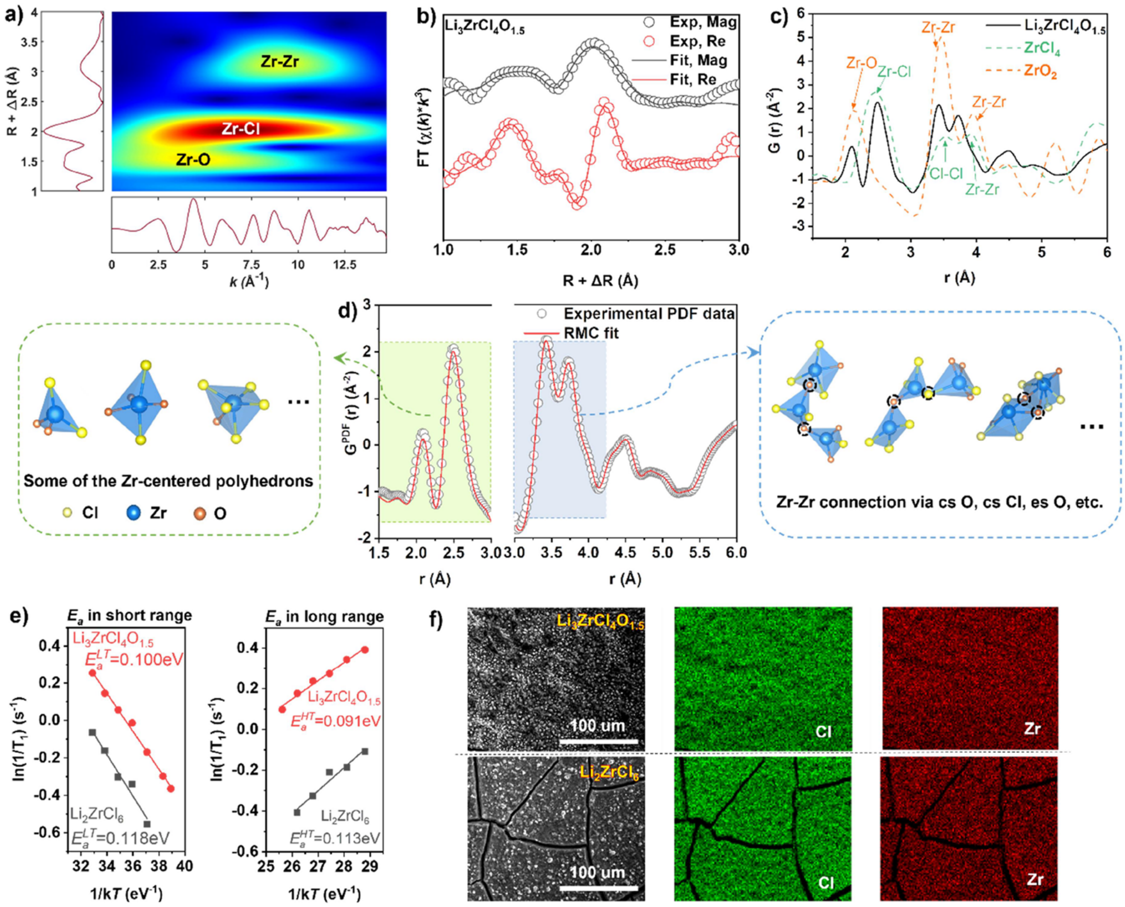

Figure 3. (a) WT spectrum of $Li_3ZrCl_4O_{1.5}$ at the Zr *K*-edge. A k^3 weighting was used. (b) FT-EXAFS fitting results for the Zr *K*-edge spectrum of the $Li_3ZrCl_4O_{1.5}$ showing the experimental data (gray circle) and Feff modeling (gray line) in terms of magnitude of FT and the real part of FT experimental data (red circle) and Feff modeling (red line) traces. (c) Comparison of the PDFs of $Li_3ZrCl_4O_{1.5}$, $ZrCl_4$, and ZrO_2. (d) RMC fit (red line) to the experimental $G(r)$ (gray circle) of $Li_3ZrCl_4O_{1.5}$. Several possible basic building blocks in $Li_3ZrCl_4O_{1.5}$ are shown on the left side. On the right side, the schemes show the connectivity that leads to the edge-sharing and corner-sharing Zr-centered polyhedra in $Li_3ZrCl_4O_{1.5}$, respectively. (e) Temperature-dependent ^{7}Li SLR NMR rates for $Li_3ZrCl_4O_{1.5}$ and Li_2ZrCl_6 measured in the laboratory frame of the reference. (f) Backscattered electron (BSE) images and the corresponding energy dispersive X-ray spectroscopy (EDS) elemental mapping for the surface of cold-pressed $Li_3ZrCl_4O_{1.5}$ and Li_2ZrCl_6 pellets, respectively.

crystalline impurity signals in $Li_3ZrCl_4O_{1.5}$ SEs were even undetectable by lab-based XRD measurements. Further increasing the amount of Li_2O (x = 0.75 and 1) led to considerable impurities of LiCl and Li_2O in addition to the amorphous main phases. At the Li/Zr molar ratio of 3:1, and improving the content of Cl or O, neither Cl-rich nor O-rich attempts could show similarly high amorphization as the $Li_3ZrCl_4O_{1.5}$ (Figure S9).

Ionic conductivities of the $Li_{2+2x}ZrCl_4O_{1+x}$ SEs (x = 0, 0.25, 0.5, 0.75, and 1) were evaluated via electrochemical impedance spectroscopy measurements. The temperature-dependent Nyquist plots are displayed in Figure S10, and the extracted ionic conductivity values at 25 °C are shown in Figure 2b. The $Li_3ZrCl_4O_{1.5}$ SE with the highest amorphization showed the highest ionic conductivity of $(1.35 \pm 0.07) \times 10^{-3}$ S cm^{-1} (at 25 °C). Arrhenius plots of $Li_{2+2x}ZrCl_4O_{1+x}$ samples were compared in Figure 2c. $Li_3ZrCl_4O_{1.5}$ showed the lowest activation energy (E_a) of 0.294 ± 0.003 eV. The trend of the activation energies implied that the structures of amorphous proportion showed a flattened energy landscape for Li-ion migration. Additionally, the electronic conductivity of the representative $Li_3ZrCl_4O_{1.5}$ SE was determined as low as 7.10 × 10^{-10} S cm^{-1} through direct current (DC) polarization measurements (Figure S11). The value was 7 orders of magnitude lower than that of the ionic conductivity, satisfying the essential requirement of electron insulation for a qualified SE. In addition, compared to the Li_2ZrCl_6 SE (5.61 × 10^{-9} S cm^{-1}), the highly amorphous $Li_3ZrCl_4O_{1.5}$ SE shows a lower electronic conductivity, which was also reported previously for the sulfide glass ceramic SE comparing to its highly crystalline one.[35]

To describe the local structure of the amorphous Zr-based halide SEs, we employed X-ray absorption near edge structure (XANES) spectroscopy. Zr *K*-edge XANES spectra of the SEs were obtained to correlate the average local chemistry with Li-ion migration in the amorphous proportion, because the line shape of the *K*-edge of a transition metal is influenced by the nearest interatomic distances of neighboring atoms.[36] Figure S12 compares the spectral features of Li_2ZrCl_6 and Li_2ZrCl_4O along with reference spectra of $ZrCl_4$ and ZrO_2 with known structures. The whiteline of Li_2ZrCl_6 showed three obvious splits, which were almost identical with the whiteline shape for $ZrCl_4$. Therefore, the noncrystalline structure in Li_2ZrCl_6 could be regarded as the fragmented *hcp*-Li_2ZrCl_6 with three kinds of distinct bond lengths (>0.18 Å between each other). In contrast, the whiteline shape of Li_2ZrCl_4O was smooth and merged, indicating that the differences of bond lengths in Zr−Cl/O polyhedrons became subtle for the O-substituted sample. Figure 2d compares the Zr *K*-edge spectra of $Li_{2+2x}ZrCl_4O_{1+x}$ SEs (x = 0, 0.5, and 1). With x increasing, the whiteline shape of the spectra changes to be more concentrated without any obvious splits. This further indicates that the nearest Zr-related bond lengths in amorphous $Li_{2+2x}ZrCl_4O_{1+x}$ materials are regular and uniform. Zr *K*-edge FT-EXAFS spectroscopy was then adopted to quantitatively understand the coordination environment around the central Zr in $Li_{2+2x}ZrCl_4O_{1+x}$ SEs (x = 0, 0.5, and 1) (Figure 2e). Based on the single scattering information from ZrO_2 and $ZrCl_4$ (Figure S4), the peaks resulting from the O and Cl scatterers around Zr can be roughly determined, which showed an intensity growth in Zr−O while a decrease in Zr−Cl. This suggests that increasing the x value in $Li_{2+2x}ZrCl_4O_{1+x}$ materials led to the replacement of more Cl anions nearest Zr cations by O anions. Consequently, there is a high possibility that the displaced Cl anions combine with Li cations to form LiCl impurity, which is consistent with the SXRD results.

In-depth structural analysis was further conducted on the representative $Li_3ZrCl_4O_{1.5}$ SE. As shown in Figure 3a, phase-uncorrected WT-EXAFS[37,38] confirmed that Zr was successively coordinated by O, Cl, and Zr at ∼1.5, 2, and 3 Å, respectively. EXAFS fitting (Figure 3b) provides average coordination information nearest to Zr in $Li_3ZrCl_4O_{1.5}$. A centered-Zr is surrounded by 2.5 oxygens at 2.07 Å and 5.6 chlorines at 2.49 Å (Table S2). RMC modeling for total scattering data was utilized to understand the structure configurations in the most amorphous $Li_3ZrCl_4O_{1.5}$ SE. As suggested in the PDF profiles in Figure 3c, the first two peaks correspond to Zr−O and Zr−Cl pairs, while the next two peaks within 3.0−4.1 Å are attributed to Zr−Zr bonding. We carried out RMC modeling on both the normalized $F(Q)$ and $G^{PDF}(r)$ of $Li_3ZrCl_4O_{1.5}$ to produce a statistical ensemble reconciling configurations (Figure S13a). The fitted data were in good agreement with the experimental data in both long-range orders and local structures (Figure S13b,c). As illustrated in Figure 3d, extracted statistical information around Zr atoms reveals basic building blocks, including $[ZrO_aCl_b]^{(2a+b-4)-}$ ($0 \leq b/a < 6$) and $[ZrCl_6]^{2-}$ polyhedrons (Figure S13d). These Zr-centered polyhedrons are predominantly connected via corner-sharing (cs) Cl (∼55%) and cs O (∼37%), with the rest exhibiting edge-sharing and a few face-sharing configurations (Figure S13e). Over 90% of Cl anions are closely surrounded by Li ions (53%) or served as terminal Cl (38%) (Figure S13f). We further performed 50 repeated RMC runs on $Li_3ZrCl_4O_{1.5}$ total scattering data, each with distinctive randomness. The small uncertainty for each of the relevant results (error bars shown in Figure S13d to f) guarantees the reliability of the RMC resulted conclusion.

The E_a for Li-ion transport in the determined local structures in $Li_3ZrCl_4O_{1.5}$ was evaluated by temperature-dependent ^7Li spin−lattice relaxation (SLR) nuclear magnetic resonance (NMR) measurements. According to the "Bloembergen, Purcell and Pound" model,[39] slopes of two-flank divisional points below the highest value of $1/T_1$ can be used to depict the E_a of Li-ion migrations in short-range (low-temperature flank, E_a^{LT}) and long-range (high-temperature flank, E_a^{HT}), respectively.[40] As shown in Figure 3e, E_a^{LT} for $Li_3ZrCl_4O_{1.5}$ was 0.100 eV, which was around 20% lower than that of Li_2ZrCl_6 (0.118 eV) with the crystalline phase dominating. The O/Cl corner-sharing Zr-based polyhedral networks also led to a lower E_a for long-range Li-ion transport (E_a^{HT} = 0.091 eV) in $Li_3ZrCl_4O_{1.5}$.

Based on the above structural analyses for the Zr-based halide SEs and corresponding ionic conduction properties, we can claim several important conclusions. First, the amorphous component in the Zr-based halides (synthesized via the one-step BM method) shows a close correlation with the Li-ion conduction behaviors. Second, enhancing the amorphization (or reducing the crystalline impurities) by changing the local structure in the Zr-based halide SEs can improve the ionic conductivity. Third, we demonstrate that the O substitution is effective to facilitate the amorphization of Zr-based halide SEs. Specifically, compared to Li_2ZrCl_6, Li_2ZrCl_4O shows disordered and distorted Zr−O/Cl polyhedrons, in which the bond length of Zr-X (X = Cl, O) is averaged to flatten the energy landscape for Li-ion migration. Furthermore, optimizing the amorphization of Zr-based halide SEs with a higher O content ($Li_3ZrCl_4O_{1.5}$) leads to the formation of corner-shared connections within Zr−Zr polyhedrons. These are predominances to induce a wide range of distortions of Li sites and lower the energy barriers for Li-ion migration.[41] So far, we have revealed several important factors to cause an improved ionic conduction in amorphous O-substituted Zr-based halide SEs. Among these scenarios, the elongation of the average bond length of Zr−Cl was also theoretically explored by Kwak et al. as one of the main reasons for the high interfacial Li-ion conduction in the crystalline O-substituted Zr-based materials.[33] Importantly, the amorphization of Zr-based halide SEs with incorporation of O and the resulting improvement in ionic conductivity can be extended to other halides based on Ta, Nb, or Hf as the central element adjacent to Zr in the periodic table, as depicted in Figure S14. While for typical halide SEs with a formula of Li_3MCl_6 (where M = Y, Er), the simple introduction of O by replacing LiCl with Li_2O reactant proves ineffective in achieving amorphization and enhancing ionic conductivity (Figure S15). This limitation may be associated with the intrinsic glass-formation capability of the central metal element.

In addition to the favorable Li-ion conduction property of the highly amorphous $Li_3ZrCl_4O_{1.5}$ SE, good mechanical deformability is an extra highlight. As displayed in Figure 3f, at low magnification (in the scale of hundreds of micrometers), the cold-pressed Li_2ZrCl_6 pellet with low amorphization shows evident cracks on the surface. In sharp contrast, the surface of the $Li_3ZrCl_4O_{1.5}$ pellet was compact and continuous, indicating the high deformability of highly amorphous materials, which was also reported before for Li−Zr−O−Cl SE by Hu et al.[32] and other amorphous SEs.[42] One important benefit derived from the good deformability of amorphous materials is the potential to minimize grain boundaries (GBs).[43] However, the influence of GBs on the delivered ionic conductivity is still elusive for halide-based SEs, because theoretically the GB effect on the ionic conduction in Li_3InCl_6 was regarded negligible.[44] Detailed studies about the mechanical properties and GBs are unfortunately beyond the scope of this work and will be investigated in our following research.

The application potential of the amorphous $Li_3ZrCl_4O_{1.5}$ SE was evaluated in ASSBs. The electrochemical stability window (ESW) of the $Li_3ZrCl_4O_{1.5}$ SE was determined via linear cyclic voltammetry (LSV) measurements, as shown in Figure S16. The high oxidation limit of 4.1 V and reduction limit of 2 V made it possible to integrate different 4 V class cathode materials. The ESW and electrochemical stability of

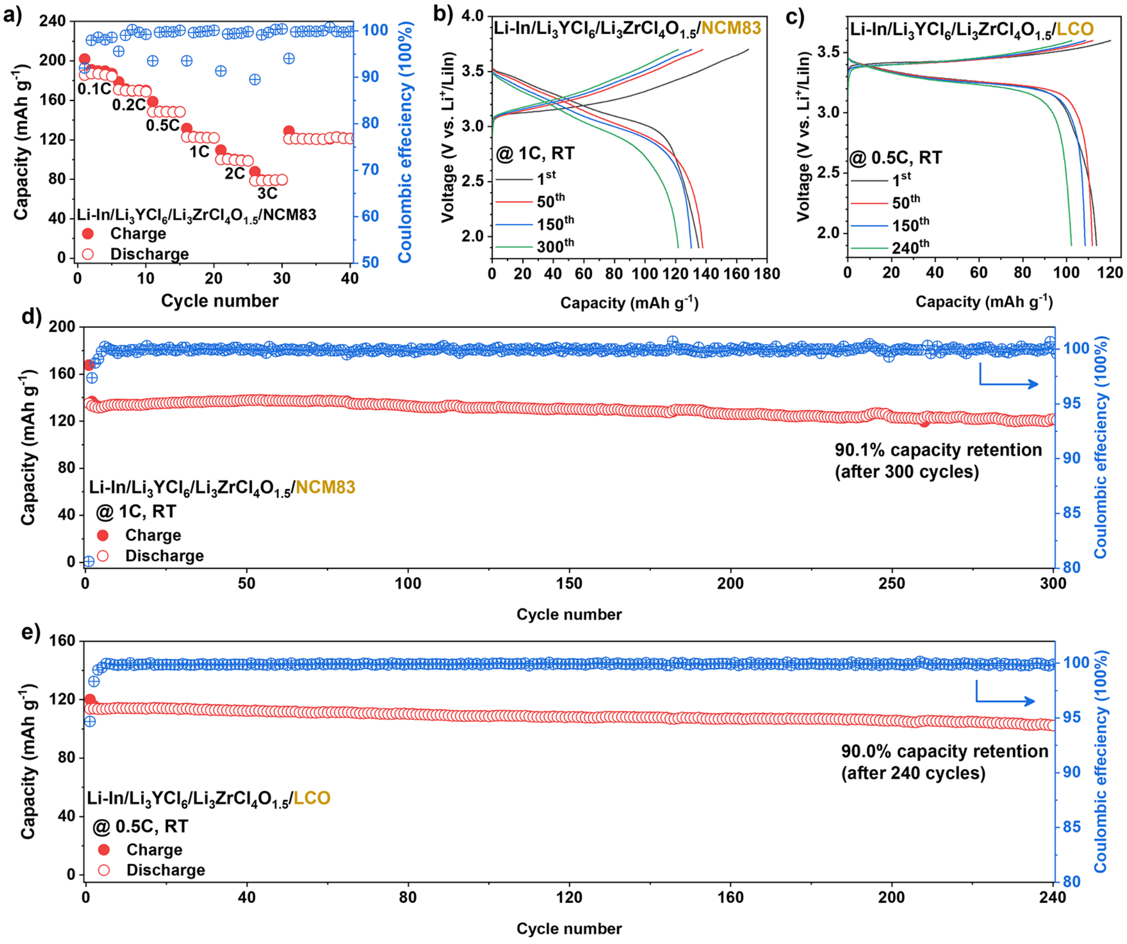

Figure 4. (a) Rate performance of ASSB with the NCM83 cathode at RT. Charge-discharge curves of the selected cycles of (b) NCM83 ASSB and (c) LCO ASSB. Cycling performances of ASSBs with (d) NCM83 cathode and (e) LCO cathode.

amorphous $Li_3ZrCl_4O_{1.5}$ was examined as superior to that of the quasi-crystalline Li_2ZrCl_6 SE. The reason is not only attributed to the benefits of incorporating O[34] and reduced electronic conductivity[35] but also is possibly related to the mechanically constrained effect of the amorphous component in SEs.[45,46] However, considering the high reduction limit of the $Li_3ZrCl_4O_{1.5}$ SE (2 V), an anode interlayer SE of Li_3YCl_6 was used to prevent direct contact between Li−In anode and $Li_3ZrCl_4O_{1.5}$ SEs.[15,18] The electrochemical performance of the constructed ASSBs with high-voltage $LiNi_{0.83}Co_{0.11}Mn_{0.06}O_2$ (NCM83) was demonstrated. As displayed in Figures 4a and S17a, an excellent rate performance was achieved. The reversible capacities of 185.7, 170.9, 148.4, 123.0, 100.1, and 78.5 mAh g^{-1} were achieved at 0.1, 0.2, 0.5, 1, 2, and 3 C (1 C = 200 mA g^{-1}), respectively. The cycling performance of the NCM83 ASSBs at large current densities was also desirable. As shown in Figure 4b,d, ASSBs could stably operate for over 300 cycles with a capacity retention of 90.1% at 1 C. Moreover, a reversible capacity of 96.6 mAh g^{-1} could be maintained after ASSB cycling over 600 times at 2 C (Figure S17b). The excellent interfacial compatibility between $Li_3ZrCl_4O_{1.5}$ and NCM83 was proved by a close observation on the interfacial composition via cryo-TEM characterizations as displayed in Figure S18, which was in contrast to the interface decomposition between Li_2ZrCl_6 and NCM83 revealed by Janek and Nazar.[28] That is to say, the incorporation of the O into the Zr-based SEs can prevent the formation of ZrO_2 as the interfacial reaction product when pairing up with Ni-rich cathode materials (e.g., NCM83). Besides the NCM83 cathode, the $LiCoO_2$ (LCO) cathode was also used for the $Li_3ZrCl_4O_{1.5}$ SE-based ASSBs. As exhibited in Figure 4c, the initial Coulombic efficiency of LCO ASSB evaluated at 0.5 C (1 C = 140 mA g^{-1}) reached 94.7, and 90.0% of the initially reversible capacity could be sustained after 240 consecutive cycles (Figure 4e).

3. CONCLUSIONS

In summary, taking the Zr-based halide SEs as an example, we successfully illustrated how the amorphous content correlates with the ionic conductivity of some lithium metal (IV or V) (oxy)halide SEs. The amorphization of Zr-based halides (SEs) can be elaborately tuned by incorporating oxygen, resulting in the amorphous content changing from 46.0 to 89.5%. An optimized composition, $Li_3ZrCl_4O_{1.5}$, was highly amorphous and showed a high ionic conductivity of $(1.35 \pm 0.07) \times 10^{-3}$ S cm^{-1} at 25 °C. Combining synchrotron-based X-ray absorption spectroscopy analysis and RMC fitting for the total scattering data, we reveal the local structures of the amorphous $Li_3ZrCl_4O_{1.5}$ SE. The distorted Zr−O/Cl polyhedrons with averaged Zr-X (X = O, Cl) bond length constitute the anion framework via a desirable O/Cl corner-sharing manner. This is regarded as the intrinsic reason for the promising ionic conductivity. In addition to the improved ionic conductivity, amorphization brings about an enhanced mechanical property. Consequently, the representative $Li_3ZrCl_4O_{1.5}$ SEs enable ASSBs operating with outstanding performance at 25 °C. This study shall provide new understandings and design principles of high-performance halide SEs, leading to a key advancement for halide-based ASSBs.

■ ASSOCIATED CONTENT

Supporting Information

The Supporting Information is available free of charge at https://pubs.acs.org/doi/10.1021/jacs.3c07343.

Experimental details include materials, methods, and characterizations. Addtional figures and tables are also provided to support the main text (PDF)

■ AUTHOR INFORMATION

Corresponding Authors

M. Danny Gu − *Eastern Institute for Advanced Study, Eastern Institute of Technology, Ningbo, Zhejiang 315200, P. R. China*; Email: m.danny.gu@gmail.com

Yuanpeng Zhang − *Neutron Scattering Division, Oak Ridge National Laboratory, Oak Ridge, Tennessee 37831, United States*; orcid.org/0000-0003-4224-3361; Email: zhangy3@ornl.gov

Graham King − *Canadian Light Source Inc., Saskatoon, SK S7N 2 V3, Canada*; orcid.org/0000-0003-1886-7254; Email: graham.king@lightsource.ca

Xueliang Sun − *Department of Mechanical and Materials Engineering, Western University, London, ON N6A 5B9, Canada; Eastern Institute for Advanced Study, Eastern Institute of Technology, Ningbo, Zhejiang 315200, P. R. China*; orcid.org/0000-0003-0374-1245; Email: xsun9@uwo.ca

Authors

Shumin Zhang − *Department of Mechanical and Materials Engineering, Western University, London, ON N6A 5B9, Canada*

Feipeng Zhao − *Department of Mechanical and Materials Engineering, Western University, London, ON N6A 5B9, Canada*

Lo-Yueh Chang − *National Synchrotron Radiation Research Centre, Hsinchu 30076, Taiwan*

Yu-Chun Chuang − *National Synchrotron Radiation Research Centre, Hsinchu 30076, Taiwan*; orcid.org/0000-0002-2879-5381

Zhen Zhang − *Department of Materials Science and Engineering, Southern University of Science and Technology, Shenzhen 518055, P. R. China*

Yuanmin Zhu − *Research Institute of Interdisciplinary Science and School of Materials Science and Engineering, Dongguan University of Technology, Dongguan 523808, China*

Xiaoge Hao − *Department of Mechanical and Materials Engineering, Western University, London, ON N6A 5B9, Canada*

Jiamin Fu − *Department of Mechanical and Materials Engineering, Western University, London, ON N6A 5B9, Canada; Department of Chemistry, Western University, London, ON N6A 5B7, Canada*

Jiatang Chen − *Department of Chemistry, Western University, London, ON N6A 5B7, Canada*; orcid.org/0000-0002-9705-6523

Jing Luo − *Department of Mechanical and Materials Engineering, Western University, London, ON N6A 5B9, Canada*

Minsi Li − *Department of Mechanical and Materials Engineering, Western University, London, ON N6A 5B9, Canada*

Yingjie Gao − *Department of Mechanical and Materials Engineering, Western University, London, ON N6A 5B9, Canada*; orcid.org/0000-0002-6853-7870

Yining Huang − *Department of Chemistry, Western University, London, ON N6A 5B7, Canada*; orcid.org/0000-0001-9265-5896

Tsun-Kong Sham − *Department of Chemistry, Western University, London, ON N6A 5B7, Canada*; orcid.org/0000-0003-1928-6697

Complete contact information is available at: https://pubs.acs.org/10.1021/jacs.3c07343

Author Contributions

◆S.Z. and F.Z. contributed equally to this work.

Notes

The authors declare no competing financial interest.

■ ACKNOWLEDGMENTS

This research was supported by the Natural Sciences and Engineering Research Council of Canada (NSERC), the Canada Research Chair Program (CRC), the Canada Foundation for Innovation (CFI), the Ontario Research Foundation (ORF), and the University of Western Ontario (UWO). The synchrotron research was performed at the Canadian Light Source, a national research facility of the University of Saskatchewan, which was supported by the CFI, NSERC, the National Research Council (NRC), the Canadian Institutes of Health Research (CIHR), the Government of Saskatchewan, and the University of Saskatchewan. This work has been partially supported by UT-Battelle, LLC, under Contract No. DE-AC05-00OR22725 with the US Department of Energy. The financial support is partially from Basic Research Foundation of Guangdong Province (Nos. 2022A1515140092 & 2023A1515011166). The TEM work used the resources of the Electron Microscopy Center from Dongguan University of Technolgy and the Cryo-TEM Center, Pico Center from SUSTech Core Research Facilities. Authors thank Sandamini H. Alahakoon from the University of Western Ontario for the assistance of NMR data collection.

■ REFERENCES

(1) Xiao, J.; Shi, F. F.; Glossmann, T.; Burnett, C.; Liu, Z. From laboratory innovations to materials manufacturing for lithium-based batteries. *Nat. Energy* **2023**, *8* (4), 329−339.

(2) Grey, C. P.; Hall, D. S. Prospects for lithium-ion batteries and beyond-a 2030 vision. *Nat. Commun.* **2020**, *11* (1), 6279.

(3) Zeng, X. Q.; Li, M.; Abd El-Hady, D.; Alshitari, W.; Al-Bogami, A. S.; Lu, J.; Amine, K. Commercialization of Lithium Battery Technologies for Electric Vehicles. *Adv. Energy Mater.* **2019**, *9* (27), No. 1900161.

(4) Janek, J.; Zeier, W. G. Challenges in speeding up solid-state battery development. *Nat. Energy* **2023**, *8*, 230−240.

(5) Zhao, Q.; Stalin, S.; Zhao, C.-Z.; Archer, L. A. Designing solid-state electrolytes for safe, energy-dense batteries. *Nat. Rev. Mater.* **2020**, *5* (3), 229−252.

(6) Chen, R.; Li, Q.; Yu, X.; Chen, L.; Li, H. Approaching practically accessible solid-state batteries: stability issues related to solid electrolytes and interfaces. *Chem. Rev.* **2020**, *120* (14), 6820−6877.

(7) Xia, W.; Zhao, Y.; Zhao, F. P.; Adair, K. G.; Zhao, R.; Li, S.; Zou, R. Q.; Zhao, Y. S.; Sun, X. L. Antiperovskite Electrolytes for Solid-State Batteries. *Chem. Rev.* **2022**, *122* (3), 3763−3819.

(8) Feng, X. Y.; Fang, H.; Wu, N.; Liu, P. C.; Jena, P.; Nanda, J.; Mitlin, D. Review of modification strategies in emerging inorganic solid-state electrolytes for lithium, sodium, and potassium batteries. *Joule* **2022**, *6* (3), 543−587.

(9) Wu, J. H.; Liu, S. F.; Han, F. D.; Yao, X. Y.; Wang, C. S. Lithium/Sulfide All-Solid-State Batteries using Sulfide Electrolytes. *Adv. Mater.* **2021**, *33* (6), No. 2000751.

(10) Liang, J. W.; Li, X. N.; Adair, K. R.; Sun, X. L. Metal halide superionic conductors for all-solid-state batteries. *Acc. Chem. Res.* **2021**, *54* (4), 1023−1033.

(11) Li, X. N.; Liang, J. W.; Yang, X. F.; Adair, K. R.; Wang, C. H.; Zhao, F. P.; Sun, X. L. Progress and perspectives on halide lithium conductors for all-solid-state lithium batteries. *Energy Environ. Sci.* **2020**, *13* (5), 1429−1461.

(12) Wang, C.; Liang, J.; Kim, J. T.; Sun, X. Prospects of halide-based all-solid-state batteries: From material design to practical application. *Sci. Adv.* **2022**, *8* (36), No. eadc9516.

(13) Kwak, H.; Wang, S.; Park, J.; Liu, Y. S.; Kim, K. T.; Choi, Y.; Mo, Y. F.; Jung, Y. S. Emerging Halide Superionic Conductors for All-Solid-State Batteries: Design, Synthesis, and Practical Applications. *ACS Energy Lett.* **2022**, *7* (5), 1776−1805.

(14) Tanaka, Y.; Ueno, K.; Mizuno, K.; Takeuchi, K.; Asano, T.; Sakai, A. New Oxyhalide Solid Electrolytes with High Lithium Ionic Conductivity > 10 mS/cm for All-Solid-State Batteries. *Angew. Chem., Int. Ed.* **2023**, *62* (13), No. e202217581.

(15) Asano, T.; Sakai, A.; Ouchi, S.; Sakaida, M.; Miyazaki, A.; Hasegawa, S. Solid halide electrolytes with high lithium-ion conductivity for application in 4 V class bulk-type all-solid-state batteries. *Adv. Mater.* **2018**, *30* (44), No. 1803075.

(16) Li, X. N.; Liang, J. W.; Luo, J.; Banis, M. N.; Wang, C. H.; Li, W. H.; Deng, S. X.; Yu, C.; Zhao, F. P.; Hu, Y. F.; Sham, T. K.; Zhang, L.; Zhao, S. Q.; Lu, S. G.; Huang, H.; Li, R. Y.; Adair, K. R.; Sun, X. L. Air-stable Li3InCl6 electrolyte with high voltage compatibility for all-solid-state batteries. *Energy Environ. Sci.* **2019**, *12* (9), 2665−2671.

(17) Liang, J. W.; Li, X. N.; Wang, S.; Adair, K. R.; Li, W. H.; Zhao, Y.; Wang, C. H.; Hu, Y. F.; Zhang, L.; Zhao, S. Q.; Lu, S. G.; Huang, H.; Li, R. Y.; Mo, Y. F.; Sun, X. L. Site-occupation-tuned superionic $Li_{(x)}ScCl_{(3+x)}$ halide solid electrolytes for all-solid-state batteries. *J. Am. Chem. Soc.* **2020**, *142* (15), 7012−7022.

(18) Zhou, L.; Zuo, T.-T.; Kwok, C. Y.; Kim, S. Y.; Assoud, A.; Zhang, Q.; Janek, J.; Nazar, L. F. High areal capacity, long cycle life 4 V ceramic all-solid-state Li-ion batteries enabled by chloride solid electrolytes. *Nat. Energy* **2022**, *7*, 83−93.

(19) Fu, J. M.; Wang, S.; Liang, J. W.; Alahakoon, S. H.; Wu, D. J.; Luo, J.; Duan, H.; Zhang, S. M.; Zhao, F. P.; Li, W. H.; Li, M. S.; Hao, X. G.; Li, X. A.; Chen, J. T.; Chen, N.; King, G.; Chang, L. Y.; Li, R. Y.; Huang, Y. N.; Gu, M.; Sham, T. K.; Mo, Y. F.; Sun, X. L. Superionic Conducting Halide Frameworks Enabled by Interface-Bonded Halides. *J. Am. Chem. Soc.* **2023**, *145* (4), 2183−2194.

(20) Yin, Y.-C.; Yang, J.-T.; Luo, J.-D.; Lu, G.-X.; Huang, Z.; Wang, J.-P.; Li, P.; Li, F.; Wu, Y.-C.; Tian, T.; Meng, Y.-F.; Mo, H.-S.; Song, Y.-H.; Yang, J.-N.; Feng, L.-Z.; Ma, T.; Wen, W.; Gong, K.; Wang, L.-J.; Ju, H.-X.; Xiao, Y.; Li, Z.; Tao, X.; Yao, H.-B. A LaCl3-based lithium superionic conductor compatible with lithium metal. *Nature* **2023**, *616* (7955), 77−83.

(21) Li, X. N.; Liang, J. W.; Chen, N.; Luo, J.; Adair, K. R.; Wang, C. H.; Banis, M. N.; Sham, T. K.; Zhang, L.; Zhao, S. Q.; Lu, S. G.; Huang, H.; Li, R. Y.; Sun, X. L. Water-Mediated Synthesis of a Superionic Halide Solid Electrolyte. *Angew. Chem., Int. Ed* **2019**, *58* (46), 16427−16432.

(22) Zhou, L. D.; Kwok, C. Y.; Shyamsunder, A.; Zhang, Q.; Wu, X. H.; Nazar, L. F. A new halospinel superionic conductor for high-voltage all solid state lithium batteries. *Energy Environ. Sci.* **2020**, *13* (7), 2056−2063.

(23) Schlem, R.; Muy, S.; Prinz, N.; Banik, A.; Shao-Horn, Y.; Zobel, M.; Zeier, W. G. Mechanochemical Synthesis: A Tool to Tune Cation Site Disorder and Ionic Transport Properties of Li3MCl6 (M = Y, Er) Superionic Conductors. *Adv. Energy Mater.* **2020**, *10* (6), No. 1903719.

(24) Kwak, H.; Han, D.; Lyoo, J.; Park, J.; Jung, S. H.; Han, Y.; Kwon, G.; Kim, H.; Hong, S. T.; Nam, K. W.; Jung, Y. S. New Cost-Effective Halide Solid Electrolytes for All-Solid-State Batteries: Mechanochemically Prepared Fe3+-Substituted Li2ZrCl6. *Adv. Energy Mater.* **2021**, *11* (12), No. 2003190.

(25) Wang, K.; Ren, Q. Y.; Gu, Z. Q.; Duan, C. M.; Wang, J. Z.; Zhu, F.; Fu, Y. Y.; Hao, J. P.; Zhu, J. F.; He, L. H.; Wang, C. W.; Lu, Y. Y.; Ma, J.; Ma, C. A cost-effective and humidity-tolerant chloride solid electrolyte for lithium batteries. *Nat. Commun.* **2021**, *12* (1), 4410.

(26) Schlem, R.; Banik, A.; Ohno, S.; Suard, E.; Zeier, W. G. Insights into the Lithium Sub-structure of Superionic Conductors Li3YCl6 and Li3YBr6. *Chem. Mater.* **2021**, *33* (1), 327−337.

(27) Sebti, E.; Evans, H. A.; Chen, H. N.; Richardson, P. M.; White, K. M.; Giovine, R.; Koirala, K. P.; Xu, Y. B.; Gonzalez-Correa, E.; Wang, C. M.; Brown, C. M.; Cheetham, A. K.; Canepa, P.; Clement, R. J. Stacking Faults Assist Lithium-Ion Conduction in a Halide-Based Superionic Conductor. *J. Am. Chem. Soc.* **2022**, *144* (13), 5795−5811.

(28) Kochetkov, I.; Zuo, T. T.; Ruess, R.; Singh, B.; Zhou, L. D.; Kaup, K.; Janek, J.; Nazar, L. Different interfacial reactivity of lithium metal chloride electrolytes with high voltage cathodes determines solid-state battery performance. *Energy Environ. Sci.* **2022**, *15* (9), 3933−3944.

(29) Ishiguro, Y.; Ueno, K.; Nishimura, S.; Iida, G.; Igarashib, Y. TaCl5-glassified Ultrafast Lithium Ion-conductive Halide Electrolytes for High-performance All-solid-state Lithium Batteries. *Chem. Lett.* **2023**, *52* (4), 237−241.

(30) Zhang, S.; Zhao, F.; Chen, J.; Fu, J.; Luo, J.; Alahakoon, S. H.; Chang, L.-Y.; Feng, R.; Shakouri, M.; Liang, J.; Zhao, Y.; Li, X.; He, L.; Huang, Y.; Sham, T.-K.; Sun, X. A family of oxychloride amorphous solid electrolytes for long-cycling all-solid-state lithium batteries. *Nat. Commun.* **2023**, *14* (1), 3780.

(31) Hayashi, A.; Hama, S.; Morimoto, H.; Tatsumisago, M.; Minami, T. Preparation of Li2S-P2S5 amorphous solid electrolytes by mechanical milling. *J. Am. Ceram. Soc.* **2001**, *84* (2), 477−479.

(32) Hu, L.; Wang, J.; Wang, K.; Gu, Z.; Xi, Z.; Li, H.; Chen, F.; Wang, Y.; Li, Z.; Ma, C. A cost-effective, ionically conductive and compressible oxychloride solid-state electrolyte for stable all-solid-state lithium-based batteries. *Nat. Commun.* **2023**, *14* (1), 3807.

(33) Kwak, H.; Kim, J.-S.; Han, D.; Kim, J. S.; Park, J.; Kwon, G.; Bak, S.-M.; Heo, U.; Park, C.; Lee, H.-W.; Nam, K.-W.; Seo, D.-H.; Jung, Y. S. Boosting the interfacial superionic conduction of halide solid electrolytes for all-solid-state batteries. *Nat. Commun.* **2023**, *14* (1), 2459.

(34) Li, B.; Li, Y.; Zhang, H.-S.; Wu, T.-T.; Guo, S.; Cao, A.-M. Fast Li+-conducting Zr4+-based oxychloride electrolyte with good thermal and solvent stability. *Sci. China Mater.* **2023**, *66* (8), 3123−3128.

(35) Wang, S.; Zhang, W. B.; Chen, X.; Das, D.; Ruess, R.; Gautam, A.; Walther, F.; Ohno, S.; Koerver, R.; Zhang, Q.; Zeier, W. G.; Richter, F. H.; Nan, C. W.; Janek, J. Influence of Crystallinity of Lithium Thiophosphate Solid Electrolytes on the Performance of Solid-State Batteries. *Adv. Energy Mater.* **2021**, *11* (24), No. 2100654.

(36) Natoli, C. R. *EXAFS and Near Edge Structure III*. In Proceedings of an International Conference, Stanford, CA, July 16−20; Hodgson, K. O.; Hedman, B.; Penner-Hahn, J. E., Eds.; Springer Berlin, Heidelberg: Stanford, CA, 1984; pp. 38−42.

(37) Xia, Z. M.; Zhang, H.; Shen, K. C.; Qu, Y. Q.; Jiang, Z. Wavelet analysis of extended X-ray absorption fine structure data: Theory, application. *Physica B* **2018**, *542*, 12−19.

(38) Munoz, M.; Argoul, P.; Farges, F. Continuous Cauchy wavelet transform analyses of EXAFS spectra: A qualitative approach. *Am. Mineral.* **2003**, *88* (4), 694−700.

(39) Bloembergen, N.; Purcell, E. M.; Pound, R. V. Relaxation Effects in Nuclear Magnetic Resonance Absorption. *Phys. Rev.* **1948**, *73* (7), 679−712.

(40) Yu, C.; Ganapathy, S.; de Klerk, N. J. J.; Roslon, I.; van Eck, E. R. H.; Kentgens, A. P. M.; Wagemaker, M. Unravelling Li-Ion Transport from Picoseconds to Seconds: Bulk versus Interfaces in an Argyrodite Li6PS5Cl−Li2S All-Solid-State Li-Ion Battery. *J. Am. Chem. Soc.* **2016**, *138* (35), 11192−11201.

(41) Jun, K.; Sun, Y.; Xiao, Y.; Zeng, Y.; Kim, R.; Kim, H.; Miara, L. J.; Im, D.; Wang, Y.; Ceder, G. Lithium superionic conductors with corner-sharing frameworks. *Nat. Mater.* **2022**, *21*, 924−931.

(42) Chi, X. W.; Zhan, Y.; Hao, F.; Kmiec, S.; Dong, H.; Xu, R.; Zhao, K. J.; Ai, Q.; Terlier, T.; Wang, L.; Zhao, L. H.; Guo, L. Q.; Lou, J.; Xin, H. L.; Martin, S. W.; Yao, Y. An electrochemically stable homogeneous glassy electrolyte formed at room temperature for all-solid-state sodium batteries. *Nat. Commun.* **2022**, *13* (1), 2854.

(43) Milan, E.; Pasta, M. The role of grain boundaries in solid-state Li-metal batteries. *Mater. Futures* **2023**, *2* (1), No. 013501.

(44) Quirk, J. A.; Dawson, J. A. Design Principles for Grain Boundaries in Solid-State Lithium-Ion Conductors. *Adv. Energy Mater.* **2023**, *13* (32), No. 2301114.

(45) Fitzhugh, W.; Ye, L. H.; Li, X. The effects of mechanical constriction on the operation of sulfide based solid-state batteries. *J. Mater. Chem. A* **2019**, *7* (41), 23604−23627.

(46) Wu, F.; Fitzhugh, W.; Ye, L. H.; Ning, J. X.; Li, X. Advanced sulfide solid electrolyte by core-shell structural design. *Nat. Commun.* **2018**, *9* (1), 4037.